

Thermoelectric Effect in Kagome Lattice Enhanced at Van Hove Singularities

Kaiki Shibata*

Graduate School of Natural Science and Technology,
Kanazawa University, Kanazawa 920-1192, Japan

Naoya Yamaguchi, Hikaru Sawahata, and Fumiyuki Ishii†

Nanomaterials Research Institute (NanoMaRi), Kanazawa University, Kanazawa 920-1192, Japan

(Dated: November 6, 2023)

We performed first-principles calculations using density functional theory on a kagome lattice model with a chiral spin state as a representative example demonstrating significant longitudinal and transverse thermoelectric properties. The results revealed that the saddle-point-type van Hove singularity (VHS) enhances thermoelectric effects. The longitudinal thermoelectric conductivity α_{xx} was large at the chemical potentials tuned close to the band at the symmetry points K (lower band edge), Γ (upper band edge), and M (saddle point), where the VHSs of the density of states were at the corresponding band energies. The transverse thermoelectric conductivity α_{xy} was large at the chemical potential of the saddle-point-type VHS. A large anomalous Nernst coefficient of approximately $10 \mu\text{V}/\text{K}$ at 50 K was expected.

I. INTRODUCTION

The thermoelectric effect is a phenomenon in which a temperature gradient generates an electric field. Seebeck and Nernst effects are two types of thermoelectric effects in which the electric field is parallel and perpendicular to the temperature gradient, respectively. The proportionality coefficients between the temperature gradient ∇T and the electric field (E) are called the Seebeck coefficient (S) and the Nernst coefficient (N), respectively, and are defined as follows:

$$S \equiv \frac{E_x}{(\nabla T)_x} = \frac{S_0 + \theta_H N_0}{1 + \theta_H^2}, \quad (1)$$

$$N \equiv \frac{E_x}{(\nabla T)_y} = \frac{N_0 - \theta_H S_0}{1 + \theta_H^2}, \quad (2)$$

where $S_0 = \alpha_{xx}/\sigma_{xx}$, $N_0 = \alpha_{xy}/\sigma_{xx}$, $\theta_H = \sigma_{xy}/\sigma_{xx}$, σ_{xx} , σ_{xy} , α_{xx} , and α_{xy} are the pure Seebeck coefficient, pure Nernst coefficient, Hall angle, electrical conductivity, Hall conductivity, longitudinal thermoelectric conductivity, and transverse thermoelectric conductivity, respectively [1, 2].

As the thermoelectric effect can potentially be applied for effectively utilizing waste heat, elucidating the origins of large S and N values can aid the development of high-performance thermoelectric devices. Equations (1) and (2) show that for a constant temperature gradient ∇T , the larger the magnitudes of S and N , the larger the magnitude of the electric field E . The numerators of Eqs. (1) and (2) indicate that large magnitudes of α_{xx} and α_{xy} result in large values of $|S|$ and $|N|$. Furthermore, α_{ij} is calculated from σ_{ij} as follows: $\alpha_{ij} = -1/|e| \int d\epsilon \sigma_{ij}(\epsilon - \mu)/T (-\partial f/\partial \epsilon)$. Based on the

semiclassical Boltzmann transport theory, σ_{xx} is given by $\sigma_{xx} = e^2 \int d\epsilon \Sigma_{xx}(\epsilon) (-\partial f/\partial \epsilon)$, where e , ϵ , μ , T , f , and Σ_{xx} are the elementary charge, energy, chemical potential, absolute temperature, Fermi-Dirac distribution function, and transport distribution function, respectively [3]. Moreover, $\Sigma_{xx}(\epsilon)$ is defined as $\Sigma_{xx}(\epsilon) = \sum_{\mathbf{k}} v_x^2(\mathbf{k}) \tau(\mathbf{k}) \delta(\epsilon - \epsilon(\mathbf{k}))$, where \mathbf{k} , v_x , τ , and δ are the wavenumber vector, group velocity in the x direction, relaxation time, and Dirac delta function, respectively [3]. If the relaxation time τ is treated as a constant, Σ_{xx} is written as $\Sigma_{xx}(\epsilon) = \tau v_x^2(\epsilon) D(\epsilon)$, where $v_x^2(\epsilon) = \sum_{\mathbf{k}} v_x^2(\mathbf{k}) \delta(\epsilon - \epsilon(\mathbf{k})) / \sum_{\mathbf{k}} \delta(\epsilon - \epsilon(\mathbf{k}))$, and the density of states (DOS) $D(\epsilon) = \sum_{\mathbf{k}} \delta(\epsilon - \epsilon(\mathbf{k}))$. In such a case, if $D(\epsilon)$ is large, we can assume that $|\alpha_{xx}|$ is large. In contrast to σ_{xx} , the anomalous Hall conductivity σ_{xy} is expressed using the wavenumber \mathbf{k} -dependent Berry curvature $\Omega_{n,z}(\mathbf{k})$ as follows: $\sigma_{xy} = e^2/\hbar \sum_n \int d^d k / (2\pi)^d \Omega_{n,z}(\mathbf{k}) f(\epsilon_n(\mathbf{k}), \mu, T)$, where n and d are the band index and the dimension of the system, respectively. Subsequently, we define the energy-dependent Berry curvature $\Omega_z(\epsilon)$ as $\Omega_z(\epsilon) = \sum_{n,\mathbf{k}} \Omega_{n,z}(\mathbf{k}) \delta(\epsilon - \epsilon_n(\mathbf{k})) / \sum_{n,\mathbf{k}} \delta(\epsilon - \epsilon_n(\mathbf{k}))$. In this case, σ_{xy} is written as $\sigma_{xy} = (e^2/\hbar) (1/V) \int d\epsilon \Omega_z(\epsilon) D(\epsilon) f(\epsilon, \mu, T)$. This shows that a large $D(\epsilon)$ is expected to yield a large $|\alpha_{xy}|$. Studies have reported that in the three-dimensional (3D) systems with nodal lines, $\text{Co}_3\text{Sn}_2\text{S}_2$, Co_2MnGa , and Fe_3Al , large $|\alpha_{xy}|$ were obtained at the energies of large $D(\epsilon)$ on the nodal lines [4].

We focused on the van Hove singularities (VHSs), which are the singularities of the DOS [5, 6], as the origin of large values of S and N . The DOS is expressed as follows: $D(\epsilon) = \int \frac{V}{(2\pi)^3} \frac{dA}{|\nabla_{\mathbf{k}} \epsilon(\mathbf{k})|}$ as the integral over the isoenergetic surface A with energy ϵ in k -space. This equation shows that the DOS has singularities at the critical points satisfying $\nabla_{\mathbf{k}} \epsilon(\mathbf{k}) = 0$. These singularities are the VHSs. Near the VHSs, the energy ϵ can be expanded into a quadratic form as a function of the wavenumber vector \mathbf{k} . We assumed that

* kaikishibata@cphys.s.kanazawa-u.ac.jp

† ishii@cphys.s.kanazawa-u.ac.jp

$\epsilon(\mathbf{k})$ is given by $\epsilon(\mathbf{k}) = \epsilon_c \pm \frac{\hbar^2}{2m_x}k_x^2 \pm \frac{\hbar^2}{2m_y}k_y^2 \pm \frac{\hbar^2}{2m_z}k_z^2$, where ϵ_c is a constant and m_x , m_y , and m_z are effective masses. In this case, the VHSs exist at $\mathbf{k} = 0$. When the signs of this equation are all negative such as $\epsilon(\mathbf{k}) = \epsilon_c - \frac{\hbar^2}{2m_x}k_x^2 - \frac{\hbar^2}{2m_y}k_y^2 - \frac{\hbar^2}{2m_z}k_z^2$, $\epsilon(\mathbf{k})$ is a maximum at $\mathbf{k} = 0$. Meanwhile, when the signs are all positive such as $\epsilon(\mathbf{k}) = \epsilon_c + \frac{\hbar^2}{2m_x}k_x^2 + \frac{\hbar^2}{2m_y}k_y^2 + \frac{\hbar^2}{2m_z}k_z^2$, $\epsilon(\mathbf{k})$ is a minimum at $\mathbf{k} = 0$. Otherwise, $\epsilon(\mathbf{k})$ is a saddle point at $\mathbf{k} = 0$. Thus, VHSs are of three types: maximum, minimum, and saddle-point types. In two-dimensional (2D) systems, near the saddle-point-type VHS ϵ_s , the DOS is expressed as follows: $D(\epsilon) \simeq -A \frac{\sqrt{m_x m_y}}{\pi^2 \hbar^2} \ln |\epsilon - \epsilon_s|$ [5, 6], which shows that $D(\epsilon)$ diverges at $\epsilon = \epsilon_s$. Thus, large $|\alpha_{xx}|$ and $|\alpha_{xy}|$ are expected at the saddle-point-type VHS. Previous studies on 2D systems such as ReX_2 ($X = \text{S, Se, Te}$) [7], FeCl_2 [8], and Fe_3GeTe_2 [9] have reported large Seebeck coefficients. Similarly, previous studies on 2D systems such as FeCl_2 [8], Fe_3GeTe_2 [9], and CrTe_2 [10] have reported large anomalous Nernst coefficients. However, there have been no discussions regarding VHSs. Therefore, this study investigated VHSs as the origin of the enhancement in S and N .

This study showed that the saddle-point type VHS yields large thermoelectric coefficients. To investigate this, we performed first-principles calculations based on the density functional theory (DFT) on the kagome lattice model with a chiral spin state. The effects of the DOS and Berry curvatures on α_{xx} and α_{xy} were investigated. Assuming a constant relaxation time, $|\alpha_{xx}|$ was found to be the maximum at the saddle-point-type VHS. Moreover, upon assuming that the intrinsic contribution was dominant in the anomalous Hall conductivity σ_{xy} , $|\alpha_{xy}|$ was the largest at the saddle-point-type VHS. Therefore, the saddle-point-type VHS was found to yield large thermoelectric coefficients in 2D magnetic materials.

II. THEORY

Using the constant relaxation time approximation, the 2D electrical conductivity σ_{xx} is given by [8, 11]:

$$\sigma_{xx}(T, \mu) = e^2 \tau \sum_n \int \frac{d^2k}{(2\pi)^2} v_{n,x}^2(\mathbf{k}) \left(-\frac{\partial f(\epsilon, \mu, T)}{\partial \epsilon} \right) \Big|_{\epsilon = \epsilon_n(\mathbf{k})} \quad (3)$$

The 2D anomalous Hall conductivity σ_{xy} induced by the Berry curvature $\mathbf{\Omega}_n(\mathbf{k}) = -i \langle \nabla_{\mathbf{k}} u_n(\mathbf{k}) | \times | \nabla_{\mathbf{k}} u_n(\mathbf{k}) \rangle$ is written as

$$\sigma_{xy}(T, \mu) = \frac{e^2}{h} \sum_n \int \frac{d^2k}{2\pi} \Omega_{n,z}(\mathbf{k}) f(\epsilon_n(\mathbf{k}), \mu, T), \quad (4)$$

where $u_n(\mathbf{k})$ is the periodic part of the Bloch function [12, 13].

The thermoelectric conductivity α_{ij} is calculated from

σ_{ij} as follows ($i, j = x$ or y) [1, 2]:

$$\alpha_{ij}(T, \mu) = -\frac{1}{|e|} \int d\epsilon \sigma_{ij}(T = 0, \epsilon) \frac{\epsilon - \mu}{T} \left(-\frac{\partial f(\epsilon, \mu, T)}{\partial \epsilon} \right). \quad (5)$$

To understand the relationship between the DOS $D(\mu)$ and α_{ij} , the Mott relation was used to express α_{ij} in terms of $D(\mu)$ as follows (refer to Appendix A for the derivation):

$$\alpha_{xx}(T, \mu) = -\frac{\pi^2 |e| k_B^2 T \tau}{3V} \frac{d}{d\mu} \left(D(\mu) v_x^2(\mu) \right), \quad (6)$$

$$\alpha_{xy}(T, \mu) = -\frac{\pi^2 |e| k_B^2 T}{3\hbar V} D(\mu) \Omega_z(\mu), \quad (7)$$

where k_B is the Boltzmann constant. For 2D systems, since the DOS diverges at the saddle-point-type VHS [5, 6], $|D(\mu)|$ and $|dD(\mu)/d\mu|$ are large. Therefore, large $|\alpha_{xx}|$ and $|\alpha_{xy}|$ are expected. At the VHSs, the Mott relation is violated for $|\alpha_{xx}|$ and $|\alpha_{xy}|$ (refer to Appendix B for more details). However, the tendency in the chemical-potential dependence of the $|\alpha_{xx}|$ and $|\alpha_{xy}|$ at the VHSs can be explained by Eqs. (6) and (7).

III. COMPUTATIONAL DETAILS

First, we performed first-principles calculations based on the density functional theory (DFT) using OpenMX (version 3.9) [14–17] to obtain eigen-energy $\epsilon(\mathbf{k})$ and Bloch wave function $\psi_{\mathbf{k}}$. To calculate a chiral spin state, we used non-collinear DFT with two-component spinor wave functions for Kohn-Sham-Bloch orbitals [18, 19]. The Kohn-Sham equation for the electrons was solved by the self-consistent field (SCF) method. The exchange-correlation potential was approximated by the generalized gradient approximation (GGA) method [20]. In OpenMX, core electrons were replaced by pseudopotentials. We used pseudo atomic orbitals as the basis function of the wave function. In this study, we constructed a kagome lattice model with a chiral spin state using hydrogen atoms. Two s-orbitals and one p-orbital were prepared as s2p1. The cutoff radius was set to 6.0 Bohr. The SCF calculations were performed by discretizing the first Brillouin zone into a $30 \times 30 \times 1$ mesh. Furthermore, the energy cutoff for the real-space numerical integrations and the solution of Poisson's equation was set to 210 Ry.

Next, the electrical conductivity σ_{xx} and anomalous Hall conductivity σ_{xy} were calculated using $\epsilon(\mathbf{k})$ and $\psi_{\mathbf{k}}$. In this calculation, we used the rigid band approximation, which assumes that the bands are invariant with respect to changes in chemical potential μ . For σ_{xx} , we obtained the values by using the semiclassical Boltzmann equation based on the semiclassical theory using Wannier90 [21–24]. In this case, $\sigma_{xx} = e^2 \int d\epsilon \Sigma_{xx}(\epsilon) (-\partial f / \partial \epsilon)$, where $\Sigma_{xx}(\epsilon)$ is the transport distribution function: $\Sigma_{xx}(\epsilon) = \sum_{\mathbf{k}} v_x^2(\mathbf{k}) \tau(\mathbf{k}) \delta(\epsilon - \epsilon(\mathbf{k}))$. For the relaxation time $\tau(\mathbf{k})$,

we considered the constant relaxation time approximation, i.e., the energy-independent relaxation time τ . In this case, we set $\tau = 10$ and 100 fs because of the relationship with σ_{xy} (refer to Appendix C for details). The velocity $v_x(\mathbf{k})$ was obtained from the Wannier function, which is the complete set of orthogonal functions, and the Fourier transform of the Bloch function. We used Wannier90 [21–24] to construct maximally-localized Wannier functions (MLWFs) for the valence bands. Velocity v_x was obtained from the Hamiltonian based on the MLWFs. Moreover, σ_{xy} was obtained from the Berry curvature, considering the case where the intrinsic contribution was dominant [25] (refer to Appendix C for details). The Berry curvature was calculated using the method proposed by Fukui, Hatsugai, and Suzuki [26]. The method was implemented in OpenMX [27, 28].

Figure D.1(a) in Appendix D shows the kagome lattice composed of the hydrogen atoms used in this calculation. The positions of the atoms were fixed. The unit cell vectors were $a_1 = a_2 = 6.60 \text{ \AA}$, and the angle between \mathbf{a}_1 and \mathbf{a}_2 was $= 120^\circ$. A slab model with a sufficient vacuum layer ($a_3 = 100 \text{ \AA}$) was used to eliminate the interactions between periodic images. To calculate the case of a chiral spin state with an azimuthal angle of 70° , we used the penalty function [29] to fix the spin orientations. Figure D.1(b) in Appendix D represents the k -space. The reciprocal lattice vectors were \mathbf{b}_1 , \mathbf{b}_2 , and \mathbf{b}_3 . The fractional coordinates of the reciprocal lattice space corresponding to the Γ , M, and K points were $(0, 0, 0)$, $(1/2, 0, 0)$, and $(1/3, 1/3, 0)$, respectively. In these coordinates, $2\pi/a$ is set to 1, where a is the length of the unit cell vector.

IV. RESULTS AND DISCUSSION

A. Electronic Structure

Figure 1(a) shows the calculated valence band structure. Three valence bands were obtained as the number of electrons per unit cell was three. We considered hole-doped cases with less than one hole. The Fermi level was within the bandwidth of the top band of the valence bands. The energy eigenvalues $\epsilon(\mathbf{k})$ are maximum, saddle point, and minimum at the Γ , M, and K points, respectively, as shown in Fig. 1(b). Figure 1(b) shows the distribution of energy eigenvalues in k -space. In the following text, the energies crossing the band at the Γ , M, and K points are denoted as E_{\max} , E_s , and E_{\min} , respectively. Figure 1(c) shows that in the energy range $E_{\min} < \epsilon < E_{\max}$, DOS $D(\epsilon)$ has three singularity points, i.e., the VHSs. The maximum, saddle, and minimum-point-type VHSs are located at $\epsilon = E_{\max}$, E_s , and E_{\min} , respectively. As our calculated system was 2D, $D(\epsilon)$ was similar to a step function at $\epsilon = E_{\min}$ and E_{\max} . At $\epsilon = E_s$, $D(\epsilon)$ diverged [5, 6].

B. Transport Properties

Figure 2(a) shows the chemical potential μ dependence (carrier-concentration dependence) of the electrical conductivity σ_{xx} at 0 K. In this case, we approximated the relaxation time τ as a constant of 10 fs. Additionally, σ_{xx} is calculated using Eq. (3). A large σ_{xx} value was obtained at $\mu = -0.15 \text{ eV}$. From Eq. (A5) in Appendix A, a large σ_{xx} value is obtained when the product of $D(\mu)$ and $v_x^2(\mu)$ are large. Figure 1(c) shows that $D(\mu)$ peaks at $\mu = E_s = -0.18 \text{ eV}$. The difference between the position of the DOS peak and that of the σ_{xx} maximum was attributed to the group velocity v_x .

Figure 2(b) shows the chemical potential μ dependence of the anomalous Hall conductivity σ_{xy} at 0 K. In this study, σ_{xy} is calculated using Eq. (4), considering the case in which the intrinsic contribution is dominant. Hereafter, we consider this case. In this case, $\sigma_{xy} = -1 (e^2/h)$ for $\mu < E_{\min}$, $\sigma_{xy} = -0.5 (e^2/h)$ for $\mu = E_s$, and $\sigma_{xy} = 0 (e^2/h)$ for $\mu > E_{\max}$. When one hole was doped, the quantized anomalous Hall conductivity $\sigma_{xy} = -1 (e^2/h)$ was obtained. In addition, the Chern numbers for the bottom, middle, and top bands were -1 , 0 , and 1 , respectively. This result is consistent with the model calculation reported by Ohgushi *et al.* [30].

To clarify the origin of σ_{xy} , we calculated the Berry curvature of the top band of the valence bands. Figure 3(a) shows the Berry curvature $\Omega_z(\mathbf{k})$ in k -space. Figure 3(b) shows the chemical-potential-dependent Berry curvature $\Omega_z(\mu)$ (refer to Eq. (A3) in Appendix A). From Fig. 3(a), $\Omega_z(\mathbf{k}) = 0$ at the Γ point, and $\Omega_z(\mathbf{k})$ is maximum at the K point. This is because the energy difference between the top and middle bands is large at the Γ point, whereas the energy difference is small at the K point, as shown in Fig. 1(a). From the relation between the energy difference and the magnitude of Berry curvature in Eq. (E1) in Appendix E, $\Omega_z(\mathbf{k})$ was expected to be small at the Γ point and large at the K point. Figure 3(a) shows that $\Omega_z(\mathbf{k}) = 0$ at the Γ point and $\Omega_z(\mathbf{k})$ is maximum at the K point. Similarly, Fig. 3(b) shows that $\Omega_z(\mu) = 0$ at $\mu = E_{\max}$ and $\Omega_z(\mu)$ is maximum at $\mu = E_{\min}$. From $\mu = E_{\min}$ to E_{\max} , where $\Omega_z(\mu)$ was large, σ_{xy} increased from $-1 (e^2/h)$ to $0 (e^2/h)$. For $\mu < E_{\min}$ and $\mu > E_{\max}$, where $\Omega_z(\mu) = 0$, σ_{xy} was constant. This is consistent with Eq. (A2) in Appendix A, where σ_{xy} is expressed in terms of $D(\mu)$ and $\Omega_z(\mu)$.

C. Thermoelectric Conductivity α_{ij}

Figure 2(c) shows the chemical potential μ dependence of the longitudinal thermoelectric conductivity α_{xx} . Large $|\alpha_{xx}|$ values were obtained at $\mu = E_{\min}$, E_s , and E_{\max} . According to Eq. (6), α_{xx} is proportional to $\frac{d}{d\mu}(D(\mu)v_x^2(\mu)) = \frac{dD}{d\mu}v_x^2 + D\frac{dv_x^2}{d\mu}$. As mentioned in Sect. I, at the saddle-point-type VHS, the DOS diverges in the 2D system. Therefore, at $\mu = E_s$, $|D|$ and $|dD/d\mu|$

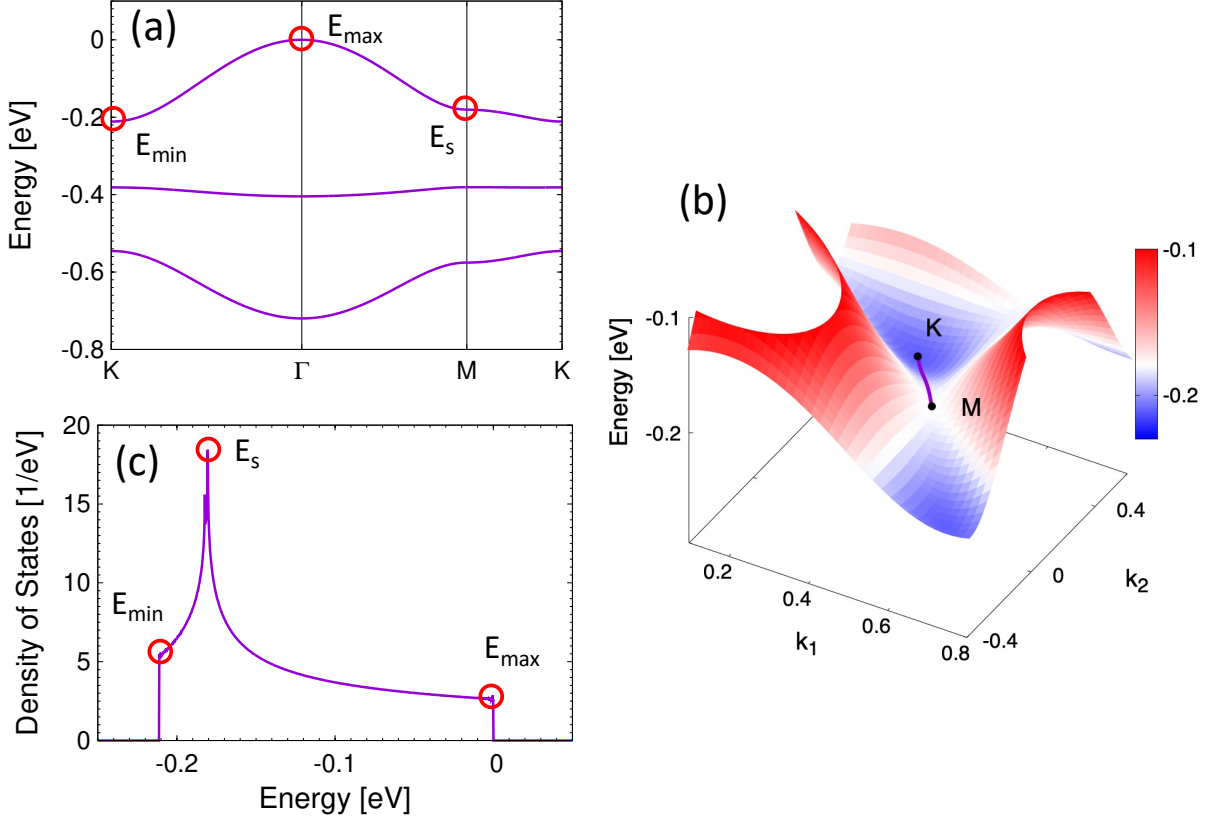


FIG. 1. (Color) (a) Band structure of the valence bands of the kagome lattice with a chiral spin state. The red circles represent the energies E_{\max} , E_s , and E_{\min} at the $\Gamma(0, 0, 0)$, $M(1/2, 0, 0)$, and $K(1/3, 1/3, 0)$ points, respectively. These points are expressed as fractional coordinates of the reciprocal lattice space with $2\pi/a$ as 1, where a is the length of the unit cell vector. We set $E_{\max} = 0$ eV. In this case, $E_s = -0.181$ eV and $E_{\min} = -0.211$ eV. (b) Distribution of energy eigenvalues in k -space for the top band of the valence bands. The z -axis represents energy eigenvalues. The contours are drawn on a linear scale from E_{\min} to -0.1 eV. The plotted energies increase from blue to red. Additionally, k_1 and k_2 are fractional coordinates of the reciprocal lattice space with $2\pi/a$ as 1. The line from the M point to the K point is the k -path of M-K in the band structure in (a). (c) Density of states of the top band of the valence bands. The maximum, saddle, and minimum-point-type VHSs are obtained at E_{\max} , E_s , and E_{\min} , respectively.

were large, resulting in the largest $|\alpha_{xx}|$ at 10 K. In contrast, for the maximum and minimum-point-type VHSs, the DOSs were similar to a step function. Therefore, $|dD/d\mu|$ was large at $\mu = E_{\min}$ and E_{\max} . Therefore, the $|\alpha_{xx}|$ values were large at the VHSs.

We obtained large $|\alpha_{xx}|$ values at the VHSs when the relaxation time τ was approximated as a constant. In the experimental studies on $\text{Bi}_2\text{Sr}_2\text{Ca}_{1-x}\text{Y}_x\text{Cu}_2\text{O}_{8+y}$ [31] and single-walled carbon nanotubes [32], the VHSs near the Fermi level were reported to enhance the Seebeck coefficients $|S|$. However, in a theoretical study on cuprate superconductors, using the energy ϵ dependent relaxation time $\tau(\epsilon)$, $|S| = 0$ when the Fermi level was at the VHSs [33]. These results indicate that the magnitude of $|\alpha_{xx}|$ may depend on the energy-dependent relaxation time $\tau(\epsilon)$ near the VHSs. Additionally, Eq. (4) reveals that the anomalous Hall conductivity σ_{xy} originating from the Berry curvature is independent of τ . Therefore, there is

no uncertainty in τ with respect to α_{xy} .

Figure 2(d) shows the chemical potential μ dependence of α_{xy} . The large $|\alpha_{xy}|$ values were obtained at $\mu = E_{\min}$ and E_s , where the VHSs and the Berry curvatures are large. First, we considered $|\alpha_{xy}|$ at the saddle-point-type VHS ($\mu = E_s$). From Eq. (7), at low temperatures, α_{xy} is proportional to the product of $D(\mu)$ and $\Omega_z(\mu)$. As $D(\mu)$ diverged at $\mu = E_s$, the largest $|\alpha_{xy}|$ was obtained at $\mu = E_s$. In addition, at $\mu = E_{\min}$, $\Omega_z(\mu)$ was the largest. Therefore, a large $|\alpha_{xy}|$ was obtained even at $\mu = E_{\min}$. In contrast, $\alpha_{xy} = 0$ at $\mu = E_{\max}$. This is because $\Omega_z(\mu) = 0$ at $\mu = E_{\max}$, as $\Omega_z(\mathbf{k}) = 0$ at the Γ point. Therefore, the product of $D(\mu)$ and $\Omega_z(\mu)$ was 0, resulting in $\alpha_{xy} = 0$. Thus, the large α_{xy} can be attributed to the VHSs and large Berry curvatures. More specifically, $|\alpha_{xy}|$ was large at $\mu = E_s$ and E_{\min} whereas $|\alpha_{xy}| = 0$ at $\mu = E_{\max}$.

Large $|\alpha_{xy}|$ were obtained at $\mu = E_{\min}$ and E_s in our computed system. We examined the condition of the

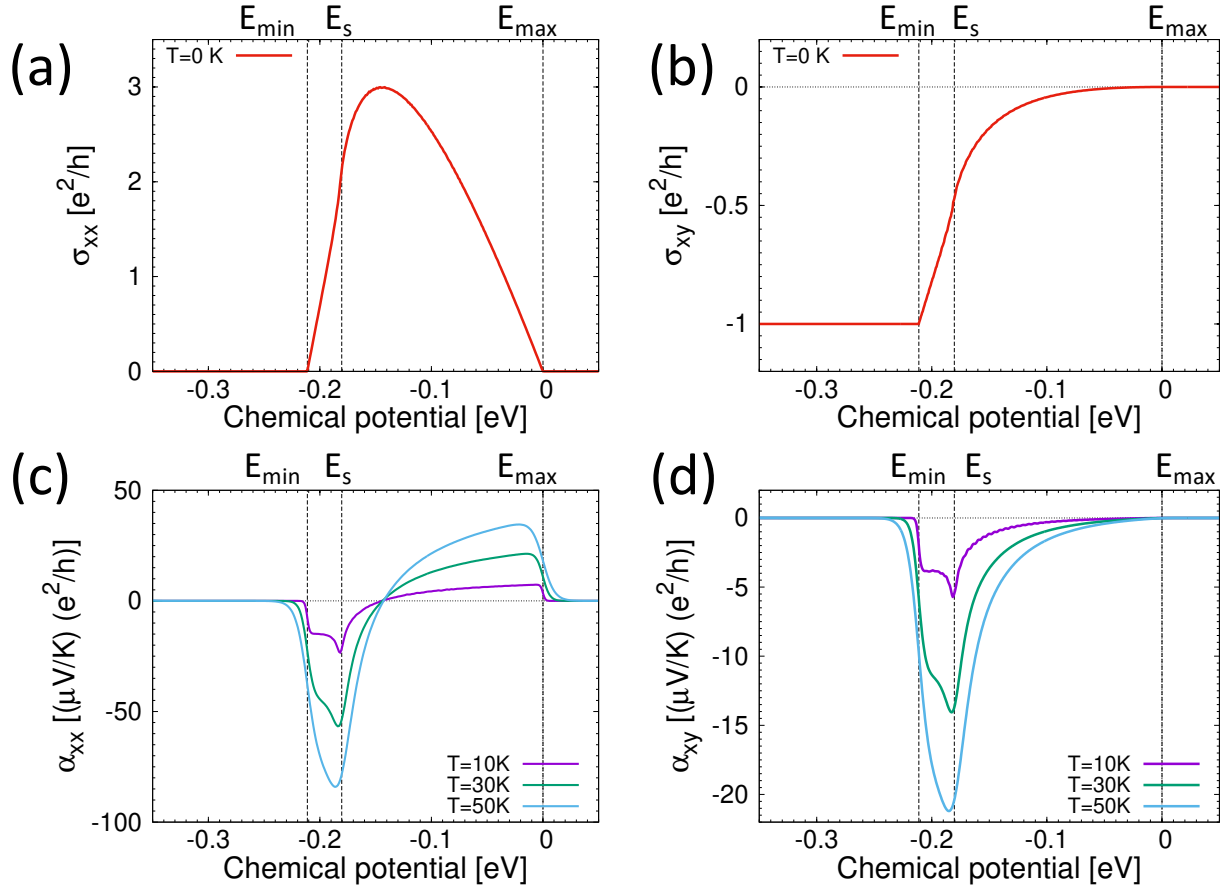


FIG. 2. (Color) Chemical potential dependence of (a) electrical conductivity σ_{xx} , (b) anomalous Hall conductivity σ_{xy} , (c) longitudinal thermoelectric conductivity α_{xx} and (d) transverse thermoelectric conductivity α_{xy} . Here, σ_{xx} and σ_{xy} correspond to $T = 0$ K, and α_{xx} and α_{xy} correspond to $T = 10, 30$, and 50 K. The relaxation time τ used to calculate σ_{xx} was approximated as a constant of 10 fs. Furthermore, E_{\min} , E_s , and E_{\max} correspond to the energies in Fig. 1.

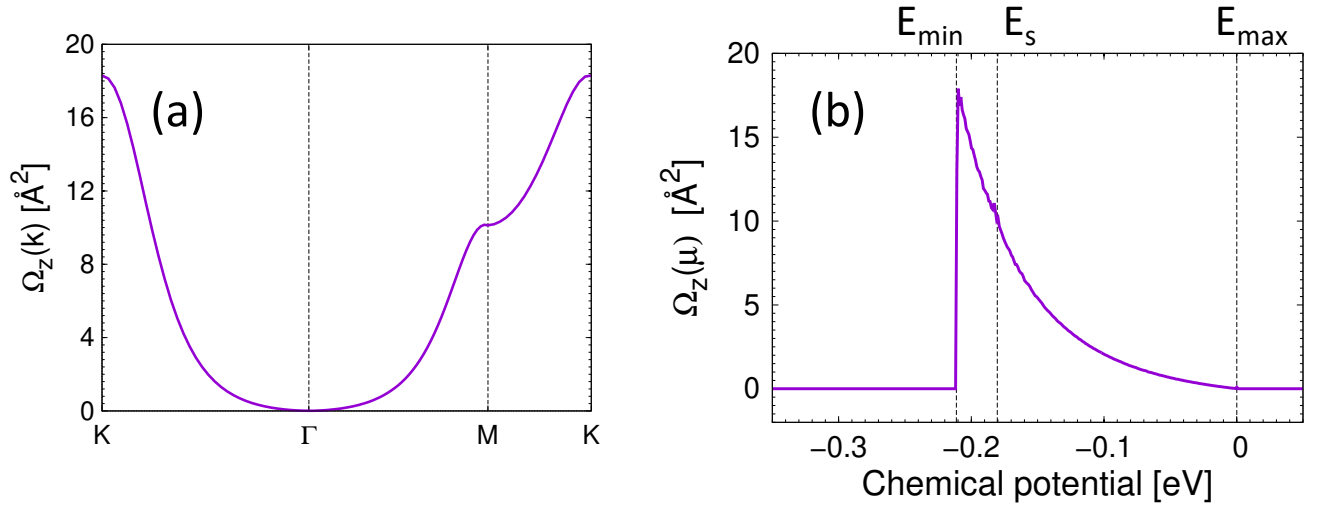


FIG. 3. (Color online) (a) Berry curvature $\Omega_z(\mathbf{k})$ in k -space on the k -path of the band structure. (b) Berry curvature $\Omega_z(\mu)$ depending on the chemical potential μ calculated using Eq. (A3) in Appendix A. Both are the Berry curvatures of the top band of the valence bands. Additionally, E_{\min} , E_s , and E_{\max} correspond to the energies in Fig. 1.

DOS and Berry curvatures that yielded large $|\alpha_{xy}|$. According to Eq. (7), both $D(\mu)$ and $\Omega_z(\mu)$ are important for the enhancement of α_{xy} , as α_{xy} is proportional to the product $D(\mu)\Omega_z(\mu)$. To obtain large $|\alpha_{xy}|$ in the range of 1.0-10 ($\mu\text{V}/\text{K}$) (e^2/h) at 10 K, the product $D(\mu)\Omega_z(\mu)$ must be in the range of 30-300 $\text{eV}^{-1} \text{\AA}^2$, as $\pi^2 ek_B^2/3\hbar V$ was approximately 4.07×10^{-3} ($\mu\text{V}/\text{K}$) (e^2/h) ($\text{eV}/\text{\AA}^2$) ($1/\text{K}$) in our case. Figure 2(d) shows that large $|\alpha_{xy}|$ is obtained at $\mu = E_{\min}$ and E_s . For $\mu = E_{\min}$, the product $D(\mu)\Omega_z(\mu)$ was $97.9 \text{ eV}^{-1} \text{\AA}^2$, as $D(E_{\min})$ was 5.47 eV^{-1} and $\Omega_z(E_{\min})$ was 17.9\AA^2 . For $\mu = E_s$, $D(\mu)\Omega_z(\mu)$ was $189 \text{ eV}^{-1} \text{\AA}^2$, as $D(E_s)$ was 18.6 eV^{-1} and $\Omega_z(E_s)$ was 10.2\AA^2 . Although $\Omega_z(\mu)$ at $\mu = E_s$ was approximately half the maximum in this band, $D(\mu)$ was the maximum resulting in large $|\alpha_{xy}|$. By contrast, at $\mu = E_{\min}$, $D(\mu)$ was less than 1/3 of E_s . As $\Omega_z(\mu)$ was maximum at E_{\min} , the product $D(\mu)\Omega_z(\mu)$ was of the same order as that of E_s . However, near $\mu = E_{\max}$, $D(\mu)\Omega_z(\mu)$ was 0 because $\Omega_z(\mu) = 0$. Thus, the large $|\alpha_{xy}|$ value originated from $D(\mu)$ was at $\mu = E_s$, whereas the magnitudes of α_{xy} originated from $\Omega_z(\mu)$ were at $\mu = E_{\min}$ and E_{\max} .

Finally, we discussed the pure Nernst coefficient $N_0 = \alpha_{xy}/\sigma_{xx}$. From Appendix C, for the saddle-point-type VHS ($\mu = E_s$), the intrinsic contribution in σ_{xy} was dominant when the relaxation time τ was in the range of 10-100 fs. Table I lists the values of σ_{xy} , τ , σ_{xx} , θ_H , and N_0 for $\mu = E_s$. Additionally, τ was assumed to be a constant of 10 or 100 fs. For $\tau = 10$ fs and $T = 50$ K, a large value of $|N_0| = 9.74 \mu\text{V}/\text{K}$ was obtained. In our calculated system, the bandwidth was 0.2 eV when the lattice constant was set to 6.6 \AA . The bandwidths of FeCl_2 [8] and CrI_3 [34], which are 2D systems reported as realistic systems, are comparable to the bandwidth reported in the present study. Therefore, large $|N_0|$ can be obtained in 2D magnetic materials. Notably, a value of $|N_0| \simeq 6 \mu\text{V}/\text{K}$ at 50 K was obtained from the first-principles calculations for FeCl_2 [8]. Furthermore, for the 3D systems Fe_3Ga and Fe_3Al , $|N|$ values of approximately $1 \mu\text{V}/\text{K}$ were obtained experimentally at 50 K [35]; our $|N_0|$ results were approximately 10 times larger than the aforementioned value.

TABLE I. Values at $\mu = E_s = -0.18$ eV

T [K]	σ_{xy} [e^2/h]	τ [fs]	σ_{xx} [e^2/h]	θ_H	N_0 [$\mu\text{V}/\text{K}$]
10	-0.459	10	2.16	-0.213	-2.45
10	-0.459	100	21.6	-0.0213	-0.245
50	-0.474	10	2.07	-0.230	-9.74
50	-0.474	100	20.7	-0.0230	-0.974

V. SUMMARY

We performed first-principles calculations based on DFT for a kagome lattice model with a chiral spin state, which is a typical model for a 2D magnetic system with a sizeable thermoelectric coefficient. First, the electronic structure was calculated; the density of states

(DOS) analysis confirmed that maximum, minimum, and saddle-point-type van Hove singularities (VHSs) were present. We investigated the contributions of the VHSs to the thermoelectric coefficients. Large $|\alpha_{xx}|$ were obtained for VHSs with constant relaxation time approximation. Large $|\alpha_{xy}|$ were obtained at the VHSs at which the Berry curvatures were large. We derived an expression for the relationship between α_{ij} and the DOS based on the Mott relation as shown in Eqs. (6) and (7). This expression shows that α_{xx} is proportional the energy derivative of $D(\epsilon)v_x^2(\epsilon)$. Similarly, α_{xy} is proportional to $D(\epsilon)\Omega_z(\epsilon)$. These expressions clearly explain α_{xx} and α_{xy} at the VHSs.

The saddle-point-type VHS is particularly essential for thermoelectric effects in 2D systems. The largest $|\alpha_{xy}|$ was obtained at the chemical potential of the saddle-point-type VHS. In our calculated system, large Nernst coefficients of 10 $\mu\text{V}/\text{K}$ at 50 K can be expected. The divergence of the DOS at the saddle-point-type VHS in 2D systems is one of the origins of large $|S|$ and $|N|$. Furthermore, 2D magnetic materials such as VSe_2 [36, 37], Cr_3Te_4 [38], CrTe [39], MnSe_x [40], Fe_3GaTe_2 [41], $\epsilon\text{-Fe}_2\text{O}_3$ [42], and CoFe_2O_4 [43] are good candidates for thermoelectric devices.

ACKNOWLEDGMENTS

This work was supported by JSPS KAKENHI (Grant Numbers JP20K15115, JP22K04862, JP22H05452, JP22H01889, and JP23H01129), JST SPRING (Grant Number JPMJSP2135), and the JST SICORP Program (Grant Number JPMJSC21E3). The computation reported in this work was conducted using the facilities of the Supercomputer Center, the Institute for Solid State Physics, the University of Tokyo.

Appendix A: Thermoelectric Conductivity Expressed in terms of the Density of States

The DOS $D(\epsilon)$ can be expressed in terms of the Dirac delta function δ using the n -th quantum state energy $\epsilon_n(\mathbf{k})$ as follows:

$$D(\epsilon) = \sum_n V \int \frac{d^3k}{(2\pi)^3} \delta(\epsilon - \epsilon_n(\mathbf{k})),$$

where V , ϵ , and k are the unit cell volume, energy, and wavenumber, respectively. The anomalous Hall conductivity $\sigma_{xy}(\mu, T)$ can be calculated from the Berry curvature $\Omega_{n,z}(\mathbf{k})$ and the Fermi-Dirac distribution function $f(\epsilon, \mu, T)$ as follows:

$$\sigma_{xy}(\mu, T) = \frac{e^2}{\hbar} \sum_n \int \frac{d^3k}{(2\pi)^3} \Omega_{n,z}(\mathbf{k}) f(\epsilon_n(\mathbf{k}), \mu, T), \quad (\text{A1})$$

where μ is the chemical potential. Changing the integrating variable in Eq. (A1) from \mathbf{k} to ϵ yields

$$\begin{aligned}\sigma_{xy}(\mu, T) &= \frac{e^2}{\hbar} \sum_n \int \frac{d^3k}{(2\pi)^3} \Omega_{n,z}(\mathbf{k}) \int d\epsilon \delta(\epsilon - \epsilon_n(\mathbf{k})) f(\epsilon, \mu, T) \\ &= \frac{e^2}{\hbar} \frac{1}{V} \int d\epsilon \left[\sum_n V \int \frac{d^3k}{(2\pi)^3} \Omega_{n,z}(\mathbf{k}) \delta(\epsilon - \epsilon_n(\mathbf{k})) \right] f(\epsilon, \mu, T) \\ &= \frac{e^2}{\hbar} \frac{1}{V} \int d\epsilon D(\epsilon) \Omega_z(\epsilon) f(\epsilon, \mu, T),\end{aligned}\quad (\text{A2})$$

where $\Omega_z(\epsilon)$ is defined as

$$\Omega_z(\epsilon) \equiv \frac{\sum_n V \int \frac{d^3k}{(2\pi)^3} \Omega_{n,z}(\mathbf{k}) \delta(\epsilon - \epsilon_n(\mathbf{k}))}{\sum_n V \int \frac{d^3k}{(2\pi)^3} \delta(\epsilon - \epsilon_n(\mathbf{k}))}.$$

At $T = 0$ K,

$$\sigma_{xy}(\mu, T = 0) = \frac{e^2}{\hbar} \frac{1}{V} \int_{-\infty}^{\mu} d\epsilon D(\epsilon) \Omega_z(\epsilon).$$

Differentiating both sides by μ results in

$$\frac{d\sigma_{xy}(\mu, T = 0)}{d\mu} = \frac{e^2}{\hbar} \frac{1}{V} D(\mu) \Omega_z(\mu).$$

Thus, the Berry curvature $\Omega_z(\mu)$ can be expressed by $d\sigma_{xy}/d\mu$ as follows:

$$\Omega_z(\mu) = \frac{\hbar V}{e^2 D(\mu)} \frac{d\sigma_{xy}(\mu, T = 0)}{d\mu}. \quad (\text{A3})$$

At low temperatures, the Mott relation [44] is a good approximation, resulting in

$$\alpha_{ij}(T, \mu) = -\frac{\pi^2 k_B^2 T}{3|e|} \left[\frac{d\sigma_{ij}(T = 0, \epsilon)}{d\epsilon} \right]_{\epsilon=\mu}, \quad (\text{A4})$$

where k_B is the Boltzmann constant. The Mott relation (Eq. (A4)) clearly indicates that α_{xy}/T is constant regardless of temperature. Some experimental results have shown that α_{xy} is proportional to $-T$ at low temperatures and $-T \ln(T)$ at high temperatures for Co_2MnGa [45], Fe_3X ($X = \text{Ga}, \text{Al}$) [35], and CoMnSb [46].

Using the Mott relation (Eq. (A4)), at low temperatures, $\alpha_{xy}(\mu, T)$ can be expressed by $D(\mu)\Omega(\mu)$ as follows:

$$\alpha_{xy}(\mu, T) = -\frac{\pi^2 |e| k_B^2 T}{3\hbar V} D(\mu) \Omega(\mu).$$

With respect to σ_{xx} , if the relaxation time τ is assumed to be constant, Eq. (3) can be expressed using $D(\mu)$ as follows:

$$\sigma_{xx}(\mu, T) = e^2 \tau \frac{1}{V} \int d\epsilon D(\epsilon) v_x^2(\epsilon) \left(-\frac{\partial f}{\partial \epsilon} \right), \quad (\text{A5})$$

where $v_x^2(\epsilon)$ is defined as

$$v_x^2(\epsilon) \equiv \frac{\sum_n V \int \frac{d^3k}{(2\pi)^3} v_{n,x}^2(\mathbf{k}) \delta(\epsilon - \epsilon_n(\mathbf{k}))}{\sum_n V \int \frac{d^3k}{(2\pi)^3} \delta(\epsilon - \epsilon_n(\mathbf{k}))}.$$

As $-(\partial f/\partial \epsilon) = \delta(\epsilon - \mu)$ at $T = 0$ K,

$$\sigma_{xx}(\mu, T = 0) = e^2 \tau \frac{1}{V} D(\mu) v_x^2(\mu).$$

Differentiating both sides by μ results in

$$\frac{d\sigma_{xx}(\mu, T = 0)}{d\mu} = e^2 \tau \frac{1}{V} \frac{d}{d\mu} \left(D(\mu) v_x^2(\mu) \right).$$

By using the Mott relation (Eq. (A4)), at low temperatures, $\alpha_{xx}(\mu, T)$ can be expressed using $D(\mu)v_x^2(\mu)$ as follows:

$$\alpha_{xx}(\mu, T) = -\frac{\pi^2 |e| k_B^2 T \tau}{3V} \frac{d}{d\mu} \left(D(\mu) v_x^2(\mu) \right).$$

Appendix B: Violation of the Mott Relation at the VHSs

From the Mott relation (Eq. (A4)), α_{xx}/T and α_{xy}/T should be constant regardless of temperature. However, Fig. B.1(a) shows that α_{xx}/T is dependent on the temperature at the VHSs ($\mu = E_{\min}$, E_s , and E_{\max}), indicating the violation of the Mott relation. Figure B.1(b) shows that α_{xy}/T was temperature dependent near the minimum-point-type VHS (E_{\min}) and the saddle-point-type VHS (E_s). Minami *et al.* [4] reported that at the VHSs derived from nodal lines, α_{xy}/T is temperature-dependent. Although no nodal line exists in our system, we obtained similar results. Furthermore, α_{xx}/T was found to be temperature-dependent at the VHSs.

Appendix C: Relaxation Time

Anomalous Hall conductivity σ_{xy} has two types of origin contributions: extrinsic and intrinsic. The extrinsic contributions are the skew scattering [47, 48] and the side jump [49, 50], whereas the intrinsic contribution is the Berry curvature [12, 13]. The anomalous Hall conductivity σ_{xy} produced by the skew scattering is proportional to the electrical conductivity σ_{xx} . In contrast, σ_{xy} produced by the side jump and Berry curvature is independent of σ_{xx} . Therefore, if the sample is clean and the temperature is low (large relaxation time), the skew scattering contribution is dominant in σ_{xy} [12, 13]. By contrast, if the sample is dirty and the temperature is high (small relaxation time), the contributions of the side jump and Berry curvature are dominant in σ_{xy} [12, 13]. Onoda *et al.* [25] reported that in the moderately dirty regime with $\sigma_{xx} \sim 3 \times 10^3 - 5 \times 10^5 \Omega^{-1} \text{cm}^{-1}$, σ_{xy} is almost constant with values of the order of $10^2 - 10^3 \Omega^{-1} \text{cm}^{-1}$.

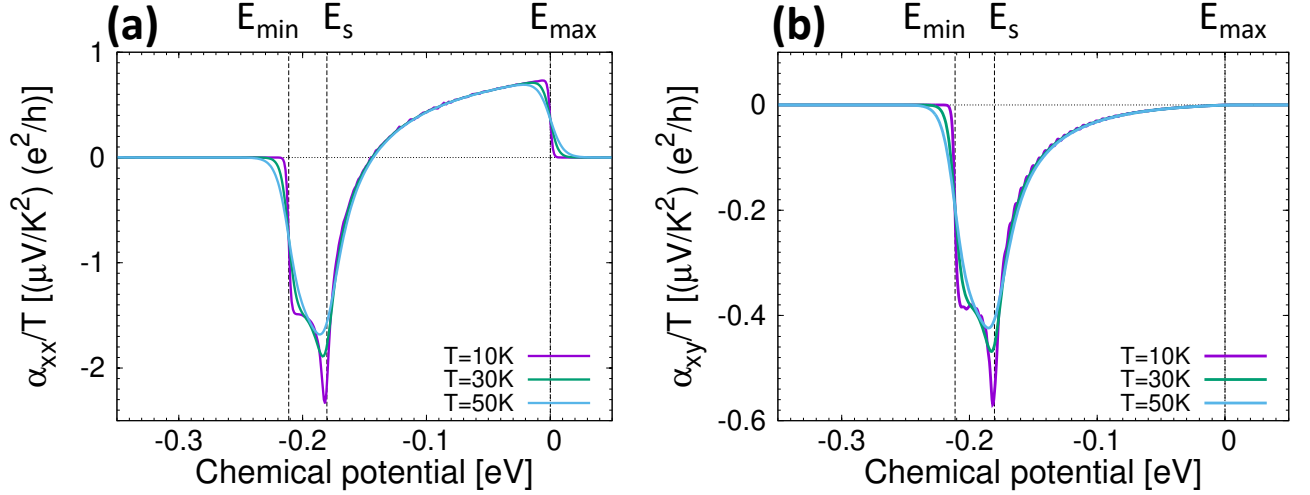


FIG. B.1. (Color) (a) Chemical potential dependence of α_{xx}/T at temperatures $T = 10, 30,$ and 50 K. Here, α_{xx}/T depends on the temperature near E_{\min} , E_s , and E_{\max} , where the VHSs were observed. The temperature dependence of α_{xx}/T is observed at E_{\min} , E_s , and E_{\max} where the VHSs were observed. In other places, α_{xx}/T is constant regardless of temperature. (b) Chemical potential dependence of α_{xy}/T . For temperatures $T = 10, 30,$ and 50 K, the values of α_{xy}/T depend on the temperature at E_{\min} and E_s . In other places, α_{xy}/T is constant regardless of temperature.

In this case, intrinsic contribution to the anomalous Hall conductivity σ_{xy} is dominant.

In our system, when the relaxation time τ was assumed to have constant values in the range $\tau = 10$ - 100 fs, the intrinsic contribution dominated in the anomalous Hall conductivity σ_{xy} . This case is consistent with the real system. As our calculated system was a monolayer, the thickness was considered to be 1 Å. In this case, at $\mu = E_s$, $\sigma_{xy} \simeq -2 \times 10^3 \Omega^{-1} \text{cm}^{-1}$. We found that $\sigma_{xx} \simeq 1 \times 10^4 \Omega^{-1} \text{cm}^{-1}$ for $\tau = 10$ fs, with the Hall angle $\theta_H = \sigma_{xy}/\sigma_{xx} \simeq -0.2$. Moreover, $\sigma_{xx} \simeq 1 \times 10^5 \Omega^{-1} \text{cm}^{-1}$ was obtained for $\tau = 100$ fs, where $\theta_H \simeq -0.02$. Therefore, for the present system, a relaxation time in the range of 10 - 100 fs was consistent with a realistic system in the moderately dirty regime in which the intrinsic contribution was dominant.

Appendix D: Computational Model

Figure D.1(a) is the computed model of the kagome lattice, and Fig. D.1(b) is the reciprocal lattice.

Appendix E: Berry Curvature and Chern Number

The components of the Berry curvature $\Omega_{n,\mu\nu}(\mathbf{k})$ can be written as a summation over the periodic part of Bloch states $|u_n(\mathbf{k})\rangle$ as follows [51, 52]:

$$\Omega_{n,\mu\nu}(\mathbf{k}) = -2\hbar^2 \text{Im} \sum_{n' \neq n} \frac{\langle u_n | v_\mu | u_{n'} \rangle \langle u_{n'} | v_\nu | u_n \rangle}{(\epsilon_n - \epsilon_{n'})^2}. \quad (\text{E1})$$

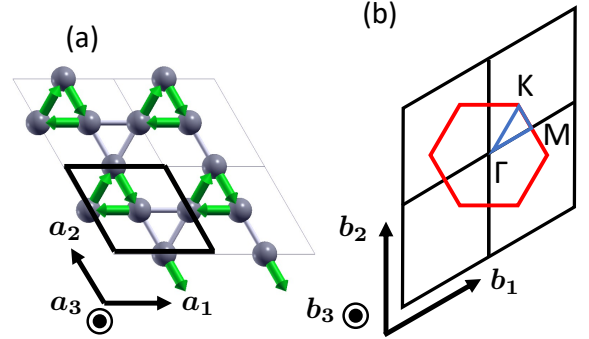


FIG. D.1. (Color) (a) Top view of the computed model of the kagome lattice. The black rhombus represents the unit cell with $a_1 = a_2 = 6.60$ Å, $a_3 = 100$ Å, $\alpha = 120^\circ$, $\beta = 90^\circ$, and $\gamma = 90^\circ$. The gray spheres represent fixed hydrogen atoms, and the gray lines represent chemical bonds. The green arrows show the spin moment, where $\mathbf{s}_1 = (\theta = 70^\circ, \phi = 60^\circ)$, $\mathbf{s}_2 = (\theta = 70^\circ, \phi = 180^\circ)$, and $\mathbf{s}_3 = (\theta = 70^\circ, \phi = 300^\circ)$. (b) The reciprocal lattice of the kagome lattice, where \mathbf{b}_1 , \mathbf{b}_2 , and \mathbf{b}_3 are the reciprocal lattice vectors. The red hexagon represents the first Brillouin zone. The fractional coordinates of the reciprocal lattice space for the Γ , M , and K points are $(0, 0, 0)$, $(1/2, 0, 0)$, and $(1/3, 1/3, 0)$, respectively. At these coordinates, $2\pi/a$ is set to 1, where a is the length of the unit cell vector.

If all bands are separated at $T = 0$ K, the anomalous Hall conductivity σ_{xy} is quantized by the Chern number ν_n in the unit of e^2/h [51, 53]. Furthermore, ν_n is calculated by integrating the Berry curvature $\Omega_{n,z}$ as fol-

lows: $\nu_n = \int \frac{d^2k}{2\pi} \Omega_{n,z}(\mathbf{k})$ [12, 13], and ν_n is always an integer. Therefore, the quantized anomalous Hall conductivity σ_{xy} at $T = 0$ K is expressed as the sum of ν_n

as follows:

$$\sigma_{xy}(T = 0) = \frac{e^2}{h} \sum_n \nu_n. \quad (\text{E2})$$

-
- [1] Y. P. Mizuta and F. Ishii, Thermopower of Doped Quantum Anomalous Hall Insulators: The case of Dirac Hamiltonian, *JPS Conf. Proc.* **5**, 011023 (2015).
- [2] Y. P. Mizuta and F. Ishii, Large anomalous Nernst effect in a skyrmion crystal, *Sci. Rep.* **6**, 28076 (2016).
- [3] G. D. Mahan and J. O. Sofo, The best thermoelectric, *Proc. Natl. Acad. Sci. USA* **93**, 7436 (1996).
- [4] S. Minami, F. Ishii, M. Hirayama, T. Nomoto, T. Koretsune, and R. Arita, Enhancement of the transverse thermoelectric conductivity originating from stationary points in nodal lines, *Phys. Rev. B* **102**, 205128 (2020).
- [5] L. Van Hove, The Occurrence of Singularities in the Elastic Frequency Distribution of a Crystal, *Phys. Rev.* **89**, 1189 (1953).
- [6] G. Grosso and G. P. Parravicini, *Solid State Physics (Second Edition)* (Academic Press Inc, 2014).
- [7] I. M. R. Verzola, R. A. B. Villaos, W. Purwitasari, Z.-Q. Huang, C.-H. Hsu, G. Chang, H. Lin, and F.-C. Chuang, Prediction of van Hove singularities, excellent thermoelectric performance, and non-trivial topology in monolayer rhenium dichalcogenides, *Mater. Today Commun.* **33**, 104468 (2022).
- [8] R. Syariati, S. Minami, H. Sawahata, and F. Ishii, First-principles study of anomalous Nernst effect in half-metallic iron dichloride monolayer, *APL Materials* **8**, 041105 (2020).
- [9] J. Xu, W. A. Phelan, and C.-L. Chien, Large Anomalous Nernst Effect in a van der Waals Ferromagnet Fe_3GeTe_2 , *Nano Lett.* **19**, 8250 (2019).
- [10] X. Yang, X. Zhou, W. Feng, and Y. Yao, Tunable magneto-optical effect, anomalous Hall effect, and anomalous Nernst effect in the two-dimensional room-temperature ferromagnet $1T-\text{CrTe}_2$, *Phys. Rev. B* **103**, 024436 (2021).
- [11] S. Minami, F. Ishii, Y. P. Mizuta, and M. Saito, First-principles study on thermoelectric properties of half-Heusler compounds CoMSb ($M = \text{Sc}, \text{Ti}, \text{V}, \text{Cr}, \text{and Mn}$), *Appl. Phys. Lett.* **113**, 032403 (2018).
- [12] D. Xiao, M.-C. Chang, and Q. Niu, Berry phase effects on electronic properties, *Rev. Mod. Phys.* **82**, 1959 (2010).
- [13] N. Nagaosa, J. Sinova, S. Onoda, A. H. MacDonald, and N. P. Ong, Anomalous Hall effect, *Rev. Mod. Phys.* **82**, 1539 (2010).
- [14] T. Ozaki, Variationally optimized atomic orbitals for large-scale electronic structures, *Phys. Rev. B* **67**, 155108 (2003).
- [15] T. Ozaki and H. Kino, Numerical atomic basis orbitals from H to Kr, *Phys. Rev. B* **69**, 195113 (2004).
- [16] T. Ozaki and H. Kino, Efficient projector expansion for the ab initio LCAO method, *Phys. Rev. B* **72**, 045121 (2005).
- [17] K. Lejaeghere, G. Bihlmayer, T. Björkman, P. Blaha, S. Blügel, V. Blum, D. Caliste, I. E. Castelli, S. J. Clark, A. Dal Corso, S. De Gironcoli, T. Deutsch, J. K. Dewhurst, I. Di Marco, C. Draxl, M. Duřak, O. Eriksson, J. A. Flores-Livas, K. F. Garrity, L. Genovese, P. Giannozzi, M. Giantomassi, S. Goedecker, X. Gonze, O. Grånäs, E. Gross, A. Gulans, F. Gygi, D. Hamann, P. J. Hasnip, N. Holzwarth, D. Iuşan, D. B. Jochym, F. Jollet, D. Jones, G. Kresse, K. Koepnik, E. Küçükbenli, Y. O. Kvashnin, I. L. Locht, S. Lubeck, M. Marsman, N. Marzari, U. Nitzsche, L. Nordström, T. Ozaki, L. Paulatto, C. J. Pickard, W. Poelmans, M. I. Probert, K. Refson, M. Richter, G.-M. Rignanese, S. Saha, M. Scheffler, M. Schlipf, K. Schwarz, S. Sharma, F. Tavazza, P. Thunström, A. Tkatchenko, M. Torrent, D. Vanderbilt, M. J. Van Setten, V. Van Speybroeck, J. M. Wills, J. R. Yates, G.-X. Zhang, and S. Cottenier, Reproducibility in density functional theory calculations of solids, *Science* **351**, aad3000 (2016).
- [18] U. von Barth and L. Hedin, A local exchange-correlation potential for the spin polarized case. i, *J. Phys. C: Solid State Phys.* **5**, 1629 (1972).
- [19] J. Kubler, K.-H. Hock, J. Sticht, and A. R. Williams, Density functional theory of non-collinear magnetism, *J. Phys. F: Met. Phys.* **18**, 469 (1988).
- [20] J. P. Perdew, K. Burke, and M. Ernzerhof, Generalized Gradient Approximation Made Simple, *Phys. Rev. Lett.* **77**, 3865 (1996).
- [21] A. A. Mostofi, J. R. Yates, Y.-S. Lee, I. Souza, D. Vanderbilt, and N. Marzari, wannier90: A tool for obtaining maximally-localised Wannier functions, *Comput. Phys. Commun.* **178**, 685 (2008).
- [22] A. A. Mostofi, J. R. Yates, G. Pizzi, Y.-S. Lee, I. Souza, D. Vanderbilt, and N. Marzari, An updated version of wannier90: A tool for obtaining maximally-localised Wannier functions, *Comput. Phys. Commun.* **185**, 2309 (2014).
- [23] H. Weng, T. Ozaki, and K. Terakura, Revisiting magnetic coupling in transition-metal-benzene complexes with maximally localized Wannier functions, *Phys. Rev. B* **79**, 235118 (2009).
- [24] G. Pizzi, D. Volja, B. Kozinsky, M. Fornari, and N. Marzari, BoltzWann: A code for the evaluation of thermoelectric and electronic transport properties with a maximally-localized Wannier functions basis, *Comput. Phys. Commun.* **185**, 422 (2014).
- [25] S. Onoda, N. Sugimoto, and N. Nagaosa, Quantum transport theory of anomalous electric, thermoelectric, and thermal Hall effects in ferromagnets, *Phys. Rev. B* **77**, 165103 (2008).
- [26] T. Fukui, Y. Hatsugai, and H. Suzuki, Chern Numbers in Discretized Brillouin Zone: Efficient Method of Computing (Spin) Hall Conductances, *J. Phys. Soc. Jpn.* **74**, 1674 (2005).
- [27] H. Sawahata, N. Yamaguchi, H. Kotaka, and F. Ishii, First-principles study of electric-field-induced topological phase transition in one-bilayer $\text{Bi}(111)$, *Jpn. J. Appl. Phys.* **57**, 030309 (2018).

- [28] H. Sawahata, N. Yamaguchi, S. Minami, and F. Ishii, First-principles calculation of anomalous Hall and Nernst conductivity by local Berry phase, *Phys. Rev. B* **107**, 024404 (2023).
- [29] P. Kurz, F. Förster, L. Nordström, G. Bihlmayer, and S. Blügel, Ab initio treatment of noncollinear magnets with the full-potential linearized augmented plane wave method, *Phys. Rev. B* **69**, 024415 (2004).
- [30] K. Ohgushi, S. Murakami, and N. Nagaosa, Spin anisotropy and quantum Hall effect in the kagomé lattice: Chiral spin state based on a ferromagnet, *Phys. Rev. B* **62**, R6065 (2000).
- [31] F. Munakata, K. Matsuura, K. Kubo, T. Kawano, and H. Yamauchi, Thermoelectric power of $\text{Bi}_2\text{Sr}_2\text{Ca}_{1-x}\text{Y}_x\text{Cu}_2\text{O}_{8+y}$, *Phys. Rev. B* **45**, 10604 (1992).
- [32] K. Yanagi, S. Kanda, Y. Oshima, Y. Kitamura, H. Kawai, T. Yamamoto, T. Takenobu, Y. Nakai, and Y. Maniwa, Tuning of the Thermoelectric Properties of One-Dimensional Material Networks by Electric Double Layer Techniques Using Ionic Liquids, *Nano Lett.* **14**, 6437 (2014).
- [33] D. M. Newns, C. C. Tsuei, R. P. Huebener, P. J. M. van Bentum, P. C. Pattnaik, and C. C. Chi, Quasiclassical Transport at a van Hove Singularity in Cuprate Superconductors, *Phys. Rev. Lett.* **73**, 1695 (1994).
- [34] M. Zhu, H. Yao, L. Jiang, and Y. Zheng, Theoretical model of spintronic device based on tunable anomalous Hall conductivity of monolayer CrI_3 , *Appl. Phys. Lett.* **116**, 022404 (2020).
- [35] A. Sakai, S. Minami, T. Koretsune, T. Chen, T. Higo, Y. Wang, T. Nomoto, M. Hirayama, S. Miwa, D. Nishio-Hamane, F. Ishii, R. Arita, and S. Nakatsuji, Iron-based binary ferromagnets for transverse thermoelectric conversion, *Nature* **581**, 53 (2020).
- [36] M. Bonilla, S. Kolekar, Y. Ma, H. C. Diaz, V. Kalappattil, R. Das, T. Eggers, H. R. Gutierrez, M.-H. Phan, and M. Batzill, Strong room-temperature ferromagnetism in VSe_2 monolayers on van der Waals substrates, *Nat. Nanotechnol.* **13**, 289 (2018).
- [37] W. Yu, J. Li, T. S. Herng, Z. Wang, X. Zhao, X. Chi, W. Fu, I. Abdelwahab, J. Zhou, J. Dan, Z. Chen, Z. Chen, Z. Li, J. Lu, S. J. Pennycook, Y. P. Feng, J. Ding, and K. P. Loh, Chemically Exfoliated VSe_2 Monolayers with Room-Temperature Ferromagnetism, *Adv. Mater.* **31**, 1903779 (2019).
- [38] R. Chua, J. Zhou, X. Yu, W. Yu, J. Gou, R. Zhu, L. Zhang, M. Liu, M. B. H. Breese, W. Chen, K. P. Loh, Y. P. Feng, M. Yang, Y. L. Huang, and A. T. S. Wee, Room Temperature Ferromagnetism of Monolayer Chromium Telluride with Perpendicular Magnetic Anisotropy, *Adv. Mater.* **33**, 2103360 (2021).
- [39] H. Wu, W. Zhang, L. Yang, J. Wang, J. Li, L. Li, Y. Gao, L. Zhang, J. Du, H. Shu, and H. Chang, Strong intrinsic room-temperature ferromagnetism in freestanding non-van der Waals ultrathin 2D crystals, *Nat. Commun.* **12**, 5688 (2021).
- [40] D. J. O'Hara, T. Zhu, A. H. Trout, A. S. Ahmed, Y. K. Luo, C. H. Lee, M. R. Brenner, S. Rajan, J. A. Gupta, D. W. McComb, and R. K. Kawakami, Room Temperature Intrinsic Ferromagnetism in Epitaxial Manganese Selenide Films in the Monolayer Limit, *Nano Lett.* **18**, 3125 (2018).
- [41] G. Zhang, F. Guo, H. Wu, X. Wen, L. Yang, W. Jin, W. Zhang, and H. Chang, Above-room-temperature strong intrinsic ferromagnetism in 2D van der Waals Fe_3GaTe_2 with large perpendicular magnetic anisotropy, *Nat. Commun.* **13**, 5067 (2022).
- [42] J. Yuan, A. Balk, H. Guo, Q. Fang, S. Patel, X. Zhao, T. Terlier, D. Natelson, S. Crooker, and J. Lou, Room-Temperature Magnetic Order in Air-Stable Ultrathin Iron Oxide, *Nano Lett.* **19**, 3777 (2019).
- [43] R. Cheng, L. Yin, Y. Wen, B. Zhai, Y. Guo, Z. Zhang, W. Liao, W. Xiong, H. Wang, S. Yuan, J. Jiang, C. Liu, and J. He, Ultrathin ferrite nanosheets for room-temperature two-dimensional magnetic semiconductors, *Nat. Commun.* **13**, 5241 (2022).
- [44] L. Smrcka and P. Streda, Transport coefficients in strong magnetic fields, *J. Phys. C* **10**, 2153 (1977).
- [45] A. Sakai, Y. P. Mizuta, A. A. Nugroho, R. Sihombing, T. Koretsune, M. Suzuki, N. Takemori, R. Ishii, D. Nishio-Hamane, R. Arita, P. Goswami, and S. Nakatsuji, Giant anomalous Nernst effect and quantum-critical scaling in a ferromagnetic semimetal, *Nat. Phys.* **14**, 1119 (2018).
- [46] H. Nakamura, S. Minami, T. Tomita, A. A. Nugroho, and S. Nakatsuji, Logarithmic criticality in transverse thermoelectric conductivity of the ferromagnetic topological semimetal CoMnSb , *Phys. Rev. B* **104**, L161114 (2021).
- [47] J. Smit, The spontaneous Hall effect in ferromagnetics I, *Physica* **21**, 877 (1955).
- [48] J. Smit, The spontaneous Hall effect in ferromagnetics II, *Physica* **24**, 39 (1958).
- [49] L. Berger, Side-Jump Mechanism for the Hall Effect of Ferromagnets, *Phys. Rev. B* **2**, 4559 (1970).
- [50] L. Berger, Application of the Side-Jump Model to the Hall Effect and Nernst Effect in Ferromagnets, *Phys. Rev. B* **5**, 1862 (1972).
- [51] D. J. Thouless, M. Kohmoto, M. P. Nightingale, and M. den Nijs, Quantized Hall Conductance in a Two-Dimensional Periodic Potential, *Phys. Rev. Lett.* **49**, 405 (1982).
- [52] Y. Yao, L. Kleinman, A. H. MacDonald, J. Sinova, T. Jungwirth, D.-s. Wang, E. Wang, and Q. Niu, First Principles Calculation of Anomalous Hall Conductivity in Ferromagnetic bcc Fe, *Phys. Rev. Lett.* **92**, 037204 (2004).
- [53] K. v. Klitzing, G. Dorda, and M. Pepper, New Method for High-Accuracy Determination of the Fine-Structure Constant Based on Quantized Hall Resistance, *Phys. Rev. Lett.* **45**, 494 (1980).